Metal-organic framework as nanoreactors to co-incorporate carbon nanodots and CdS quantum dots into the pores for improved H2 evolution without noble-metal cocatalyst

Xiang-Bin Meng, Jing-Li Sheng, Hong-Liang Tang, Xiao-Jun Sun*, Hong Dong, Feng-Ming Zhang*

Key Laboratory of Green Chemical Engineering and Technology of College of Heilongjiang Province, College of Chemical and Environmental Engineering, Harbin University of Science and Technology, Harbin, 150040, PR China

ARTICLE INFO

ABSTRACT

Avoiding the utilization of noble-metal cocatalyst and the aggregation of nano photocatalysts in the preparation and photocatalytic reaction are two important aspects in the area of photocatalytic H_2 evolution. In this work, for the first time, CdS quantum dots and carbon nanodots (CDs) were successfully co-immobilized in the cages of MIL-101 by one-step double solvents method followed by heating treatment. The optimum photocatalytic H_2-evolution rate of CD/CdS@MIL-101(50) composite with CDs content of 5.2 wt% exhibits a H_2 evolution rate of 14.66 μmol h^{-1} without noble metal assisted under visible-light irradiation, which is 8.5 and 18.6 times higher than that of CdS@MIL-101 and bare CdS, respectively. The improved photocatalytic H_2-production activity of CD/CdS@MIL-101 ternary composite is predominantly attributed to the effect of CDs, which mainly serves as an electron collector to efficiently prolong the lifetime of the photogenerated charge carriers from CdS@MIL-101 heterostructure. This work provide a new strategy of one-step double solvents method to co-incorporate two functional species to the pores of metal-organic frameworks (MOFs) to improve the photocatalytic H_2 evolution activity of host photocatalyst.

1. Introduction

Photocatalytic hydrogen evolution by water splitting with semiconductor material has been recognized as one of the most promising solutions to the global energy and environment crisis, owing to its renewable solar energy source and clean chemical fuel product [1,2,3,4]. Thus, enormous efforts have been invested to develop high efficient photocatalysts for H_2 evolution that can effectively harvest visible light, hinder the recombination of photogenerated charge, boost the rate of photogenerated electrons to H^+ [5,6,7]. Besides, pursuing low-cost photocatalysts without the participation of noble metal is another important aspect for further application of photocatalysts [8,9,10]. In recent years, metal-organic frameworks (MOFs), as a class of porous and crystalline materials composed of metal ions and organic linkers, have been proved to be a new type of promising photocatalysts for CO_2 reduction, organic syntheses and H_2 evolution [11,12,13,14,15,16]. Moreover, the intrinsic porous structure, high surface area and hybrid nature of MOFs offer special opportunities for further tuning and functionalization to endow the resulting materials with boosting activities [17,18,19]. The pore space of MOFs can serve as orderly arrayed nanoreactors, and the functional species can be synthesized and encapsulated into the pores of MOFs within these reactors to construction interesting interaction system between the host framework and guest species [20,21].

Previously, various metal nanoparticles, metal oxides and metal sulfides have been successfully incorporated into MOFs by using the pore as confine reactors. function [22,23,24,25,26,27,28]. Because the pores of MOFs are mainly below server nanometer, the sizes of the resulting loaded species are small and in the range of quantum dots [29,30]. In recent years, CdS nanoparticles have been loaded into the pores of MOFs by a typical solvents method to construct CdS@MOF heterostructure photocatalyst [31,32]. The merit of this way is that it can effectively avoid the aggregation of the nanoparticles during the synthesis and reaction processes. Besides, the guest CdS nanoparticles can construct heterostructure with the MOFs to improve the separation of photogenerated charges and thus leading to an improved photocatalytic activity of the resulting material with Pt as cocatalyst [33,34]. More recently, CDs have been recognized as a promising alternative cocatalyst for applications in photocatalysis, which low-cost, low-toxicity, excellent photostability and high solubility in aqueous solution
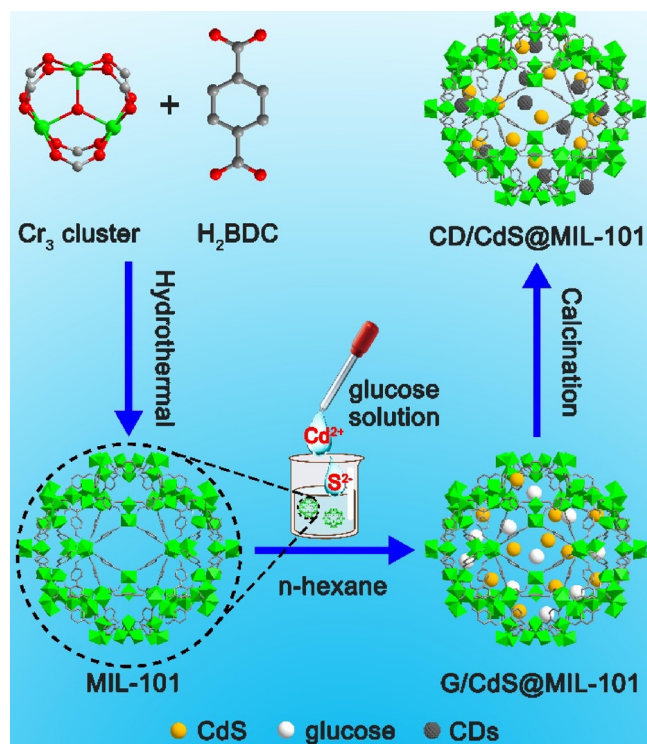

Scheme 1. Schematic illustration of the synthesis of CD/CdS@MIL-101 material.

[35,36,37]. However, the attempt of co-encapsulating CdS quantum dots and CDs into the pores of MOFs to construct a ternary nonnoble-metal composite for photocatalytic H_2 evolution has not been reported until now.

In this work, for the first time we co-incorporated CdS quantum dots and CDs into the pores of MOF to construct a ternary composite by using the pores of MOF as nanoreactors. In the synthesis process, Cd^{2+}, S^{2-} and the precursor of CDs were introduced into the pores of MIL-101 by an one-step double solvents method followed by heating treatment (Scheme 1). It was confirmed that CdS quantum dots and CDs with the size around 3 nm were uniform distributed in the pores of MIL-101. The resulting CD/CdS@MIL-101 ternary composites exhibits a improved photocatalytic H_2 evolution rate of 14.66 μmol h^{-1} which is 8.5 and 18.6 times higher than that of CdS@MIL-101 and bare CdS, respectively. The improved photocatalytic H_2-production activity of CD/CdS@MIL-101 ternary composite is predominantly attributed to the effect of CDs, which mainly serves as an electron collector to efficiently prolong the lifetime of the photogenerated charge carriers from CdS@MIL-101 heterostructure.

2. Experimental

2.1. Materials and general methods

All of the reagents and solvents were commercially available and used without further purification. The characteristics of the materials were investigated by Fourier transform infrared (FTIR) spectra (Spectrum 100), X-ray powder diffraction (XRD) patterns (Bruker D8 X-ray diffractometer). N_2 adsorption-desorption isotherms were determined by Micromeritics ASAP 2020 analyzer at 77 K. Before the measurement, the catalysts were degassed at 120 °C for 24 h. Scanning electron microscopy (SEM) micrographs (Hitachi S-4800), the transmission electron microscopy (TEM) experiment (JEM-2100 electron microscope), diffuse reflectance UV–vis spectroscopy techniques (Lambda 35 spectrometer), and thermogravimetric analyses (TGA/

SDTA851e), photoluminescence spectrum (PL) and time-resolved PL (SPEX Fluorolog-3 spectrofluorometer), X-ray photoelectron spectroscopy (XPS) techniques (Kratos-AXIS ULTRA DLD apparatus). The electrochemical impedance spectra (EIS), Mott-Schottky plot and photocurrent-time (I-T) profiles was recorded on the CHI660E electrochemical workstation with a standard three-electrode system with the photocatalyst-coated ITO as the working electrode, Pt plate as the counter electrode, and Ag/AgCl electrode as a reference electrode, A 300 W Xenon lamp with a 420 nm cut-off filter was used as the light source during the measurement. A 0.25 M Na_2SO_4 solution was used as the electrolyte. The as-synthesized samples (2 mg) were added into 1 mL ethanol and 10 μL Nafion mixed solution, and the working electrodes were prepared by dropping the suspension (200 μL) onto an ITO glass substrate electrode surface and dried at room temperature.

2.2. Synthesis of MIL-101

For a typical synthesis process, 1.9958 g of $Cr(NO_3)_3·9H_2O$ (2.4 mmol) and 0.8281 g terephthalic acid (2.4 mmol) were added to water (35 mL) and the mixture stirred for 10 min. The resulting suspense on was heated under autogenous pressure at 220 °C for 8 h in a 50 mL Teflon-lined autoclave and then cooled to room temperature. The mixture was filtered and the powder MIL-101 was isolated as a green powder following centrifugation at 8000 rpm for 10 min, and subsequently washed with ethanol at 90 °C for 12 h twice to remove unreacted terephthalic acid. Ion exchange was carried out by dispersing the solid in 150 mL of NH_4F aqueous solution (0.3 M) with stirring for 10 h at 70 °C and subsequently washed with ethanol at 90 °C for 12 h. The final green powder was vacuum dried at 150 °C and stored in a dry cabinet for further use.

2.3. Synthesis of CdS

1.85 g of $Cd(Ac)_2·2H_2O$ was dispersed in 20 mL of distilled water. Afterwards, with 20 mL of 1.66 g $Na_2S·9H_2O$ aqueous solution added into the suspension drop by drop, yellow precipitates gradually appeared. After vigorous stirring, the suspension was transferred into a Teflon-lined autoclave and held at 180 °C for 12 h. After that, the precipitates from the mixture were filtered and rinsed with distilled water, ethanol several times. The final product was dried at vacuum dried at 80 °C for 6 h

2.4. Synthesis of CdS@MIL-101

Supported CdS nanoparticles were prepared double-solvents method. Typically, 100 mg of activated MIL-101 was suspended in 20 mL of dry n-hexane as hydrophobic solvent and the mixture was sonicated for 15 min until it became homogeneous. After stirring of 2 h, 0.15 mL of $Cd(Ac)_2$ aqueous solution was added dropwise over a period of 15 min with constant vigorous stirring. After stirring of 2 h, 0.15 mL of Na_2S aqueous solution was added dropwise over a period of 15 min with constant vigorous stirring. The resulting solution was continuously stirred for 12 h. After careful filtration, the green powder was dried in air 80 °C for 12 h. Then the suspension was transferred into a Teflon-lined autoclave and held at 180 °C for 12 h. The nominal weight ratios of MIL-101 to CdS were 10%. Then the CdS@MIL-101 was dried at vacuum-dried at 80 °C for 6 h.

2.5. Synthesis of CDs@MIL-101

Supported CDs nanoparticles were prepared double-solvents method. Typically, 100 mg of activated MIL-101 was suspended in 20 mL of dry n-hexane as hydrophobic solvent and the mixture was sonicated for 15 min until it became homogeneous. After stirring of 2 h, 0.3 mL of glucose solution (10, 30, 50, and 70 mM) was added dropwise over a period of 30 min with constant vigorous stirring. The resulting

solution was continuously stirred for 12 h. After careful filtration, the green powder was dried in N_2 80 °C for 12 h. Then the nanoparticles were calcined at 200 °C under N_2 atmosphere for 2 h to transform glucose into CDs, the resulting products were labeled as CD@MIL-101(X) (X = 10, 30, 50 and 70 mM).

2.6. Synthesis of CD/CdS@MIL-101

Typically, 100 mg of activated MIL-101 was suspended in 20 mL of dry n-hexane as hydrophobic solvent and the mixture was sonicated for 15 min until it became homogeneous. After stirring of 2 h, 0.15 mL of $Cd(Ac)_2$ glucose aqueous solution with different concentration of solution as solvent (10, 30, 50, and 70 mM) was added dropwise over a period of 15 min with constant vigorous stirring. After stirring of 2 h, 0.15 mL of aqueous Na_2S·glucose solution (10, 30, 50, and 70 mM) was added dropwise over a period of 15 min with constant vigorous stirring. The resulting solution was continuously stirred for 12 h. After careful filtration, the green powder was dried in N_2 80 °C for 12 h. Then the nanoparticles were calcined at 200℃ under N_2 atmosphere for 2 h to transform glucose into CDs, and transferred into a Teflon-lined autoclave and held at 180 °C for 12 h. After the powder was dried at vacuum-dried at 80 °C for 6 h, the resulting products were labeled as CD/CdS@MIL-101(X) (X = 10, 30, 50 and 70 mM).

2.7. Photocatalytic hydrogen evolution

The photocatalytic hydrogen evolution by water splitting was performed in a glass reaction cell with quartz cover connected to a closed gas circulation and the gas circulation was swept by high purity N_2 before illumination. The 30 mg ternary composite photocatalyst or 3 mg CdS were dispersed in 50 mL of 10 vol % lactic acid aqueous solution. To thoroughly remove the air inside and make sure that the reaction system was under anaerobic conditions, the whole system was vacuumed for at least 30 min with vacuum bump before irradiation using a 300 W Xe lamp with a 420 nm cut-off filter. The reaction solution was stirred continuously and cooled to 6 °C by a flow of tap water. The amount of hydrogen evolved was determined at an interval of 1 h with online gas chromatography.

3. Results and discussion

3.1. Structure and morphology

MIL-101 was synthesized according to the reported method. The G/CdS@MIL-101(G represents glucose) was synthesized by a facile double solvent method, one-step injecting slight water solutions containing glucose (with different concentration (10, 30, 50 and 70 mM)), $Cd(Ac)_2$ and Na_2S (corresponding to 10 wt% CdS) into *n*-hexane solution containing the activated sample of MIL-101 with violent stirring. Afterwards, the obtained G/CdS@MIL-101 was calcined at 200 °C under N_2 atmosphere for 2 h to transform glucose into CDs. The main reason and advantage of using double solvent in this work to co-encapsulate CdS and CDs are as follows: Firstly, based on the hydrophilic character of the pores of MIL-101, the double solvents method could maximumly encapsulate the CdS and CDs (or its precursor) into the pores of MIL-101 to build a material with core-shell structure; Secondly, the pores of MIL-101 act as confine reactors leading to the resulting particle sizes of CdS and CDs in the range of quantum dots and avoiding the aggregation of the nanoparticles. Moreover, the one-step method can lead the uniform distribution of CdS and CDs in the pores of MIL-101.

The corresponding photos for all the samples indicate that colors of the resulting materials after CDs loading change from green to yellow and to dark brown with increasing amounts of CDs (Figure S1). As shown in Fig. 1a, image of scanning electron microscopy (SEM) indicates that the as-synthesized MIL-101 displays octahedral nanocrystals with the sizes in the range of 300–500 nm. After loading CDs and

CdS particles, the morphology of the resulting CD/CdS@MIL-101 is similar to that of its parent MIL-101 beside the surface of the nanocrystals become slightly rough (Fig. 1b). The images of element mapping for the ternary CD/CdS@MIL-101 material show that C, Cr, Cd and S are densely distributed the entire material suggesting that the CdS nanoparticles were successfully prepared and well-distributed in the pores of MIL-101 framework (Figure S2). As shown in Fig. 1c, the image of transmission electron microscopy (TEM) of CD/CdS@MIL-101 clearly show that ultra small nanoparticles were incorporated into the nanocrystals of MIL-101. The high-resolution transmission electron microscopy (HRTEM) measurements were carried out to further characterize CDs and CdS in CD/CdS@MIL-101 nanocrystals. The HRTEM image indicates that the particle size of CdS particles is around 3 nm and the (002) crystallographic planes of hexagonal CdS with a lattice spacing of 0.336 nm (Fig. 1d and S3). The amorphous CDs also can be observed with a rather narrow size around 3 nm. The amorphous character of CDs is in accord with the reported literatures that the pyrolysis temperature below 300 ° C for the organic precursors will result in amorphous particles of CDs [35]. Differently, the sizes of CdS particles without the confine of the pores of MIL-101 are about 50–80 nm with a serious aggregation (Figure S4).

The structure of as-synthesized sample was confirmed by Fourier transform infrared (FT-IR) spectroscopy and powder X-ray diffraction (PXRD) analysis. The IR absorbance peaks of CDs at 3456 and 1722 cm^{-1} are attributed to the stretching vibrations of O−H and C−O, implying the existence of hydroxyl groups (Figure S5); In addition, the absorbance peaks at 1402 and 1031 cm^{-1} can be assigned to the asymmetric and symmetric stretching vibrations of C−O−C, respectively [29]. In the FT-IR spectra of CD@MIL-101and CD/CdS@MIL-101, the peaks around 1030 cm^{-1} from CDs can clearly be observed demonstrating the formation of CDs in these composites.

As shown in Figure S6, the PXRD signals of MIL-101 well matched with its simulated patterns and combined with FT-IR Spectra (Figure S7), indicating the successful synthesis of the framework. For bare CdS prepared under similar condition without the anticipation of MIL-101, the peaks at 24.9°, 26.6°, 28.3°, 43.7°, 47.9°, and 51.9° are related to (100), (002), (101), (110), (103), and (112) crystal planes (JCPDS No.: 41-1049), respectively (Figure S8). The PXRD patterns of CdS@MIL-101 show the entire characteristic signal of hexagonal CdS and MIL-101, indicating that the CdS was successfully deposited and the structure integrity of MIL-101 after CdS loading. The PXRD patterns of CD@MIL-101 are similar to its parent MOF for the low content and the amorphous character of CDs (Figure S9) [35]. The PXRD peaks of the resulting CD/CdS@MIL-101 are also comparable to that of CdS@MIL-101 and cannot observe the signals from CDs (Fig. 2a).

The porosities of as-synthesized samples were evaluated by N_2 absorption and desorption experiments at 77 K. All of the absorption isotherms exhibit type I isotherm according to the IUPAC classification (Figs. 2b and S10). The pure MIL-101 shows the highest Brunauer-Emmett-Teller (BET) surface area of 2787 m^2 g^{-1} and pore volume of 1.31 cm^3 g^{-1}. After the encapsulation of CdS and CDs, the corresponding BET, pore volume and pore sizes (Figure S11) of the resulting materials apparently decrease [38]. The BET surface area and pore volume for CdS@MIL-101 are 1340 m^2 g^{-1} and 0.56 cm^3 g^{-1}, while these for CD@MIL-101(50) are 2105 m^2 g^{-1} and 0.92 cm^3 g^{-1}, respectively. As shown in table S1, the resulting CD/CdS@MIL-101 exhibit the lowest BET and pore volume and these values decrease with the increasing of the concentration of the glucose, which is in agreement with the fact that the pore space of MIL-101 was filled with CDs and CdS nanoparticles. The elemental composition and elemental states of CD/CdS@MIL-101 (50) were characterized by X-ray photoelectron spectroscopy (XPS). The XPS survey spectrum indicates that the elements of C, O, Cr, Cd and S exist in the CD/CdS@MIL-101(50) (Figure S12), and the elemental composition is in good agreement with the target composition. The survey spectrum clearly shows the Cd 3d and S 2p transitions. In addition, the peaks of Cd 3d are observed at 405.1 and
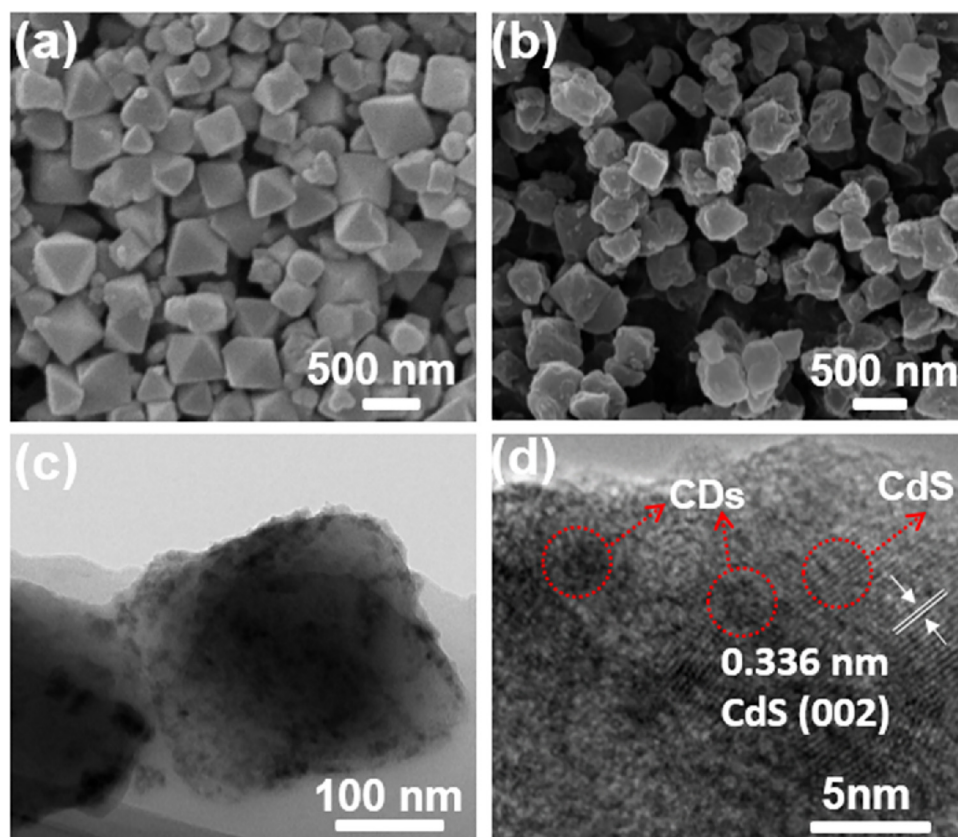
Fig. 1. (a–b) SEM images of MIL-101 and CD/CdS@MIL-101. (c–d) TEM image and HRTEM image of CD/CdS@MIL-101.

411.9 eV, which are attributed to Cd $3d_{5/2}$ and Cd $3d_{3/2}$ for Cd^{2+} state in the samples in Fig. 2c [39]. Fig. 2d shows that the S $2p_{3/2}$ and S $2p_{1/2}$ peaks are observed at 161.4 and 162.4 eV for the materials, in agreement with the expectation that sulfur existed as the sulfide species (S^{2-})

[40]. The above results further confirmed that the as obtained CD/CdS@MIL-101(50) sample is contained with CdS.

Thermogravimetric analysis (TGA) curves of MIL-101, CD@MIL-101(50) and CD/CdS@MIL-101(50) under N_2 atmosphere are displayed
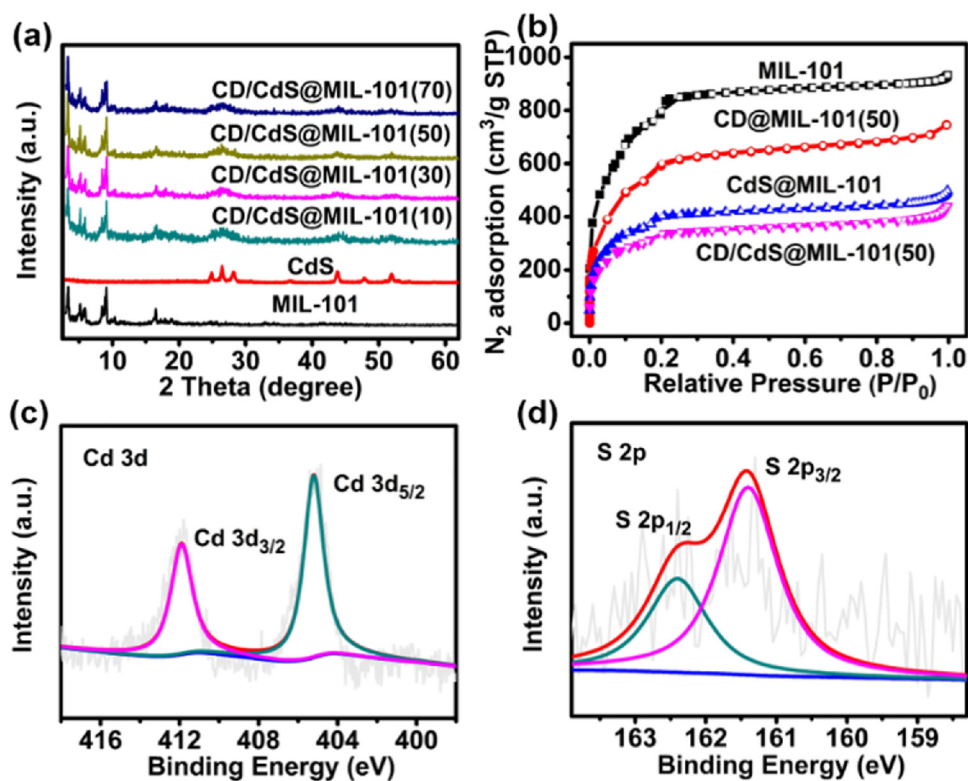

Fig. 2. (a) PXRD patterns of CdS, MIL-101, and a series of CD/CdS@MIL-101 (X). (b) N_2 absorption isotherms of MIL-101, CdS@MIL-101, CD@MIL-101(50) and CD/CdS@MIL-101(50). Filled and open symbols represent adsorption and desorption branches, respectively. (c–d) XPS spectrums of Cd 3d and S 2p of CD/CdS@MIL-101 (50).

in Figure S13. For MIL-101, three main weight loss steps are observed. The first stage weight loss is around at 100 °C due to loss of water molecules on its surface. The second step falling within the range of 125–300 °C corresponds to the loss of guest water molecules from the large cages and medium-sized cages. The third stage weight loss at 350 °C corresponds to the elimination of OH/F groups, which is followed by the decomposition of the frameworks [41]. This analysis shows the thermal stability of MIL-101, indicating the excellent thermal stability of MIL-101 during calcination at 200 °C. The TGA curve of CD@MIL-101 is similar to that its parent MIL-101 except for different weight loss at different temperature area. From the result of TGA of MIL-101 and CD@MIL-101(50), the resulting content of CDs in CD/CdS@MIL-101(50) was calculated to be about 5.2 wt% by residual quantity. The result of X-ray spectroscopy (EDS) also shows that the content of C of CD@MIL-101 apparently higher than that of its parent MIL-101, demonstrating the successful loading of CDs (Figure S14 and S15).

3.2. Photocatalytic measurement and electrochemical measurement

UV-Vis diffuse reflectance spectra (DRS) were utilized to determine the optical properties of MIL-101, CdS and the CD/CdS@MIL-101 (50) samples (Fig. 3a). CdS displays a visible light absorption with an absorption edge at ~ 550 nm which can be attributed to the intrinsic band gap absorption of hexagonal CdS. MIL-101 exhibits two characteristic absorption band centered at 450 nm and 600 nm, which coincides with that reported in literature [42]. The absorbance spectrum of CD/CdS@MIL-101 shows a combination of the spectral features of pure CdS and MIL-101, and it exhibits a sharp absorption edge rise at about 550 nm and a broad absorption in visible light region. Besides, the visible light absorption of the ternary CD/CdS@MIL-101 material has no apparent improvement compare with CdS@MIL-101 material, which may be due to the fact that the CDs is encapsulated in the pore of MIL-101 and contains only about 5 wt% (Figure S16).The corresponding band gaps for CdS and MIL-101 were calculated to be 2.32 and 2.40 eV, respectively (Figure S17). The electronic band structures of CdS, MIL-101 and CDs were further investigated by examining Mott-Schottky plots. As shown in Fig. 3b and S18, all of the samples were exhibited positive slopes in the Mott-Schottky plots at frequencies of 1000 Hz, which was an indication of the n-type semiconductors [43]. The results reveal that flat band potentials of CdS, MIL-101 and CDs are -0.74 V, -0.65 V and -0.40 V Vs Ag/AgCl at pH = 6.6, respectively. The CB potential of CdS, MIL-101 and CDs is -0.64 V, -0.55 V and -0.30 V Vs NHE (Normal hydrogen electrode) [44], which is equivalent to -3.80 eV, -3.89 eV and -4.14 eV according to the reference standard for which 0 V versus equals -4.44 eV versus evac (vacuum level) [45,46,47,48]. Combined with the band gap energy, the valence band (VB) position of CdS and MIL-101 can be calculated to be -6.12 eV and -6.29 eV Vs evac (vacuum level), respectively, suggesting that CdS@MIL-101 material showsthe type II heterojunction [49].

The photocatalytic H_2 evolution of as-synthesized samples was evaluated in lactic acid aqueous solution under visible light irradiation in the absence of precious-metal species (Fig. 3c and S19). Under the above conditions, no H_2 was detected for MIL-101 and CD/MIL-101(50), while bare CdS displays a low photocatalytic activity with a hydrogen production rate of 0.79 μmol h^{-1}. A higher hydrogen generation rate of 1.73 μmol h^{-1} was obtained for CdS@MIL-101, which is 2.2 times higher than that of pure CdS. When CDs and CdS were co-incorporated in to the pores of MIL-101, the CD/CdS@MIL-101 ternary catalysts present remarkably improved H_2 production activities. In all the CD/CdS@MIL-101 ternary catalysts with different CDs content, CD/CdS@MIL-101(50) shows the maximum H_2 evolution rate of 14.66 μmol h^{-1}, which is over 8.5 times higher than that of CdS@MIL-101 and even 18.6 times higher than CdS. The performance of different loading amounts of CdS was investigated when MIL-101 and the concentration of glucose of 50 mM are unchanged. The results show that

photocatalytic performance of 10 wt% CdS loading amounts is better than that of 5 wt% or 15 wt% CdS (Figure S20). The main probable reason is that CdS component in the composite that mainly accounts for the visible-light harvesting and too much CdS may prevent the loading CDs, resulting in decrease of H_2 evolution rate in the composite. In order to investigate the stability of the as-prepared photocatalyst, the time courses of photocatalytic H_2 evolution on CD/CdS@MIL-101(50) sample were carried out. As shown in Fig. 3d, the H_2 evolution rate of CD/CdS@MIL-101(50) composites has no apparent decrease after the fourth reaction runs. Besides, the PXRD patterns and morphology of CD/CdS@MIL-101(50) are no obvious change before and after photocatalytic reaction (Figure S21-23). These results further demonstrate the durable stability of CD/CdS@MIL-101(50) in the photocatalytic reaction.

To confirm the different roles played by the three components, physical mixtures consisting of CdS and MIL-101 with the same mass ratios as in the composites are named as CdS/MIL-101 through grinding under room temperature, and their photocatalytic properties were also researched. The SEM image of the CdS/MIL-101 shows that the as-synthesized CdS was out of the MIL-101 surface and just exist independently with large size (Figure S24). Photocatalytic activity of CdS@MIL-101 is approximately 1.6 and 2.2 times higher than that of CdS/MIL-101 (1.06 μmol h^{-1}) and CdS (0.79 μmol h^{-1}). In order to confirm the role of CDs, we prepared CD/CdS (5.2 wt% CDs) composite and tested its photocatalytic activity at the same condition. It shows that the H_2 evolution rate of CD/CdS is 3.72 μmol h^{-1}, over 4.7 times higher than that of CdS (Figure S25). Besides, The photocatalytic H_2 production rate of CD/CdS@MIL-101(50) is the highest compared with that of CD/CdS and CdS@MIL-101.

The photocurrent measurement was used to reflect the interface charge separation efficiency and the higher photocurrent intensity often leads to better photocatalytic activity [23]. Fig. 3e shows that the transient photocurrent response of CD/CdS@MIL-101(50) is higher than CdS@MIL-101 and CdS under visible-light irradiation for several on-off cycles, indicating that the CD/CdS@MIL-101(50) holds stronger ability in generating and transferring the photoexcited charge carrier under light irradiation with CDs as cocatalysts. The electron-transfer efficiency at the electrodes made from CD/CdS@MIL-101(50) was further confirmed by the electrochemical impedance spectroscopy (EIS) [50]. Further, experimental EIS data fitted to the equivalent Randle circuit using Zview software (Table S2). Obviously, the CD/CdS@MIL-101(50) has a smaller radius of curvature than that of CdS@MIL-101 and CdS (Fig. 3f), meaning the more efficient charge separation occurred after the introduction of reduced CDs.

Photoluminescence (PL) spectra of as-synthesized samples were subsequently measured to examine the recombination of photo-generated electron-hole pairs [51]. Figure S26 shows the PL spectra of MIL-101, CdS@MIL-101 and CD/CdS@MIL-101(50) monitored at an excitation wavelength of 380 nm. The pure MIL-101 sample exhibits a strong emission peak at 480 nm. In comparison, the fluorescence peak intensity of CdS@MIL-101 significant decreases clearly, indicating the heterojunctions between CdS and MIL-101 more efficient inhibition of electron-hole pairs recombination. Particularly, the ternary composite CD/CdS@MIL-101(50) presents the lowest fluorescence peak intensity among all samples, suggesting that the recombination of photo-generated electron-hole pairs is further inhibited, which may be ascribed to the inhibiting role of CDs nanoparticles. Time-resolved PL decay profiles of MIL-101, CdS@MIL-101 and CD/CdS@MIL-101(50) at 480 nm emission in Figure S27 show that both the fast and slow components of the fluorescence lifetime in CD/CdS@MIL-101(50) ($\tau_1 = 0.59$ ns 68.1%; $\tau_2 = 3.37$ ns 31.9%) are shortened as compared with those of CdS@MIL-101 ($\tau_1 = 0.63$ ns 69.9%; $\tau_2 = 3.61$ ns 30.1%) and MIL-101 ($\tau_1 = 0.68$ ns 69.6%; $\tau_2 = 4.13$ ns 30.4%). The average lifetime of CD/CdS@MIL-101(50) hybrids is 2.46 ns that is shorter than those of CdS@MIL-101 ($\tau = 2.75$ ns) and MIL-101 ($\tau = 3.23$ ns). This is because CDs can effectively accept the electrons transferred from CdS@MIL-101
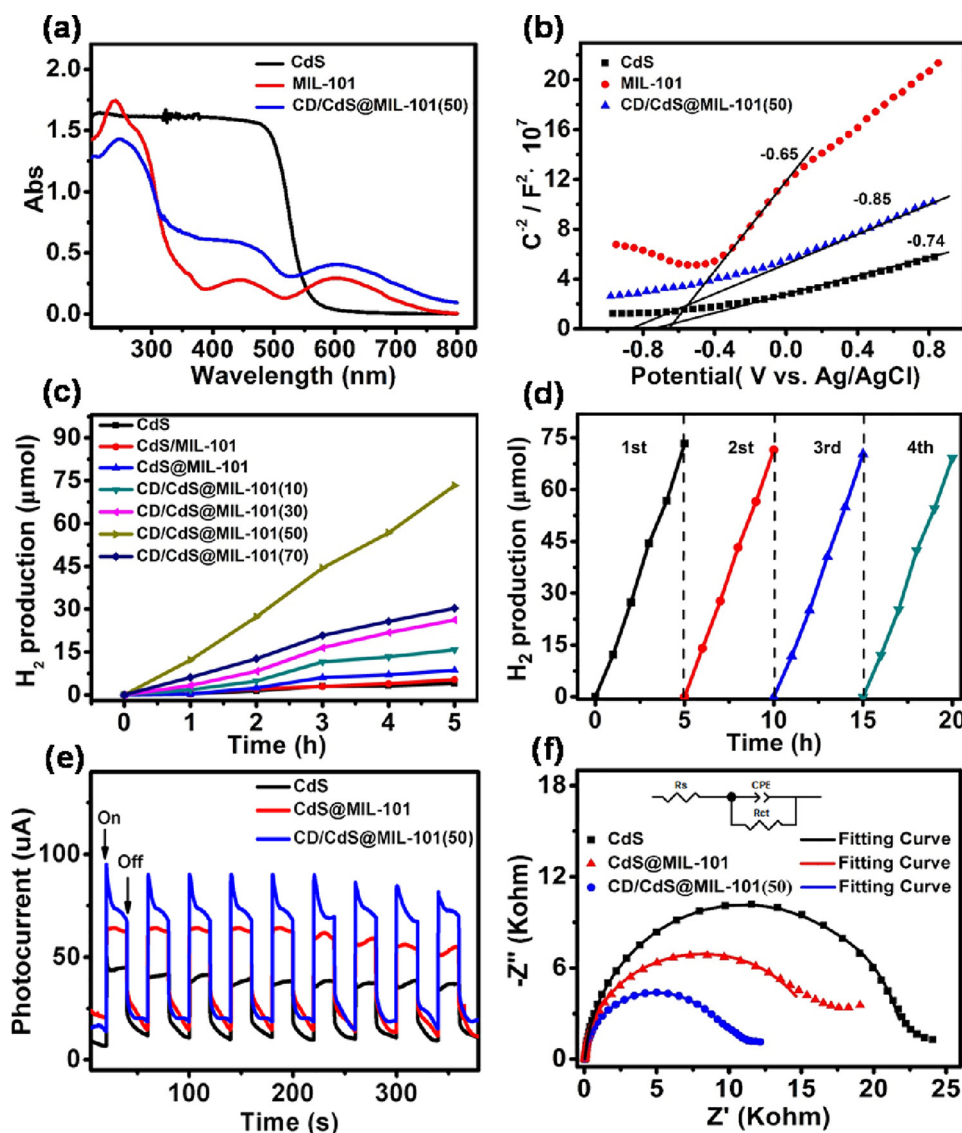
Fig. 3. (a) UV/Vis diffuse reflectance spectra and (b) Mott-Schottky plots for CdS, MIL-101 and CD/CdS@MIL-101(50). (c) Hydrogen evolution profiles of CdS, CdS/MIL-101, CdS@MIL-101 and CD/CdS@MIL-101(X) under visible light ($\lambda \geq 420$ nm). (d) Time courses for photocatalytic hydrogen production over CD/CdS@MIL-101(50) (30 mg photocatalyst was dispersed in 50 mL of 10 vol% lactic acid aqueous solution). (e–f) The photocurrent and EIS Nyquist plots for CdS, CdS@MIL-101, CD/CdS@MIL-101(50).
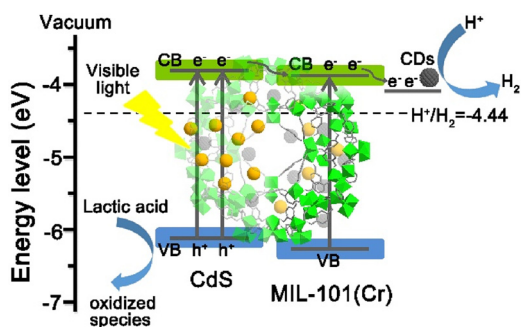

Fig. 4. Mechanism schematic of CD/CdS@MIL-101.

composites and add another decay channel to the excited states of the CdS@MIL-101. To calculate the electron transfer rate (k_{ET}), we assume that the average PL lifetimes of the CdS, CdS@MIL-101 and CD/CdS@MIL-101(50) are given by $\tau_{MIL-101} = 1/k$, $\tau_{CdS@MIL-101} = 1/(k + k_{ET1})$ and $\tau_{CD/CdS@MIL-101(50)} = 1/(k + k_{ET2})$, respectively [52,53]. The k_{ET1} and k_{ET2} can be calculated to be 5.4×10^7 s^{-1} and 9.7×10^7 s^{-1},

respectively. Through the comparison of the value of k_{ET1} and k_{ET2}, the value of k_{ET2} is larger than that of k_{ET1}, which indicates that CDs as charge collector can effectively transfer photogenerated electrons of CdS@MIL-101 composites. Both the decrease of Nyquist radius of curvature, PL intensity, PL lifetime and without significantly improved of UV–vis absorption of the ternary CD/CdS@MIL-101 composite compare with CdS@MIL-101 material, suggesting CDs mainly serves as an electron collector to efficiently prolong the lifetime of the photogenerated charge carriers from CdS@MIL-101 heterostructure.

3.3. Photocatalytic mechanism

On the basis of above results, a possible mechanism for the high H$_2$ production performance and efficient electron-hole separation in the CD/CdS@MIL-101 is proposed in Fig. 4. In the CD/CdS@MIL-101, the componet of CdS possesses excellent light absorbtance ability and acts as a light-harvest role upon visible light irradiation. Thus, under the visible light irradiation, CdS is excited to generate electrons in the CB and holes in the VB. The photogenerated electrons by CdS could be first be delivered to CB of MIL-101. Then, CDs particles are mainly regarded

as electron cisterns to facilitates the photogenerated electrons from the CB of MIL-101 transferring to H$^+$ to realize the reduction reaction, while the holes leaved in the VB of CdS are captured by lactic acid [54,55,56].

4. Conclusion

In summary, CDs and CdS quantum dots were successfully co-introduced into the pores of porous MIL-101 by a one-step double solvents method followed by heat treatment. The ternary CD/CdS@MIL-101 material exhibits apparently improved photocatalytic H$_2$ evolution activity with the optimized H$_2$ production rate of 14.66 μmol h^{-1} without any noble metal cocatalysts, which is 8.5 times higher than that of CdS@MIL-101 and even 18.6 times higher than bare CdS. Also the CD/CdS@MIL-101(50) composites exhibit stable performance during the photocatalytic reaction as confirm by the PXRD and SEM measure for the sample after reaction. The results of Nyquist curves, PL spectra, time-resolved PL spectroscopy and photocurrent measurements demonstrate that the separation efficiency of photogenerated charges of CD/CdS@MIL-101 was markedly improved for the construction of CdS and MIL-101 heterojunction as well as the function from CDs as cocatalyst. Considering the porous nature of MOFs, the strategy of one-step encapsulating two functional species into pores of MOFs can be applied to various MOFs to endow the resulting material with the aimed activity.

Conflicts of interest

There are no conflicts of interest to declare.

Acknowledgements

Appendix A. Supplementary data

Supplementary material related to this article can be found, in the online version, at doi:https://doi.org/10.1016/j.apcatb.2018.11.018.

References

[1] D. Kim, K.K. Sakimoto, D.C. Hong, P.D. Yang, Angew. Chem. Int. Ed. 54 (2015) 3259–3266.
[2] Q.P. Lu, Y.F. Yu, Q.L. Ma, B. Chen, H. Zhang, Adv. Mater. 28 (2016) 1917–1933.
[3] Z.Y. Yin, B. Chen, M. Bosman, X.H. Cao, J.Z. Chen, B. Zheng, H. Zhang, Small 10 (2014) 3537–3543.
[4] M.S. Dresselhaus, I.L. Thomas, Nature 414 (2001) 332–337.
[5] X. Wang, K. Maeda, A. Thomas, K. Takanabe, G. Xin, J.M. Carlsson, K. Domen, M. Antonietti, Nat. Mater. 8 (2009) 76–80.
[6] M. Wen, K. Mori, Y. Kuwahara, T. An, H. Yamashita, Appl. Catal., B 218 (2017) 555–569.
[7] A. Indra, A. Acharjya, P.W. Menezes, C. Merschjann, D. Hollmann, M. Schwarze, M. Aktas, A. Friedrich, S. Lochbrunner, A. Thomas, M. Driess, Angew. Chem. Int. Ed. 56 (2017) 1653–1657.
[8] M. Liu, Y. Chen, J. Su, J. Shi, X. Wang, L. Guo, Nat. Energy 1 (2016) 16151.
[9] Q. Xiang, J. Yu, M. Jaroniec, J. Am. Chem. Soc. 134 (2012) 6575–6578.
[10] J. Ran, J. Zhang, J. Yu, S.Z. Qiao, ChemSusChem 7 (2014) 3426–3434.
[11] Z.G. Gu, H. Fu, T. Neumann, Z.X. Xu, W.Q. Fu, W. Wenzel, L. Zhang, J. Zhang, C. Woll, Acs Nano 10 (2016) 977–983.
[12] K.G.M. Laurier, F. Vermoortele, R. Ameloot, D.E. De Vos, J. Hofkens, M.B.J. Roeffaers, J. Am. Chem. Soc. 135 (2013) 14488–14491.
[13] X. Fang, Q. Shang, Y. Wang, L. Jiao, T. Yao, Y. Li, Q. Zhang, Y. Luo, H.L. Jiang, Adv. Mater. 30 (2018) 1705112.
[14] Y. Chen, D. Wang, X. Deng, Z. Li, Y. Chen, D. Wang, X. Deng, Z. Li, Catal. Sci. Technol. 7 (2017).
[15] X. Deng, Z. Li, H. García, Chemistry 23 (2017) 11189.
[16] A. Dhakshinamoorthy, Z. Li, H. Garcia, Chem. Soc. Rev. 47 (2018) 8134–8172.
[17] H.C. Zhou, J.R. Long, O.M. Yaghi, Chem. Rev. 112 (2012) 673–674.
[18] J.R. Long, O.M. Yaghi, Chem. Soc. Rev. 38 (2009) 1213–1214.
[19] H. Furukawa, K.E. Cordova, M. O'Keeffe, O.M. Yaghi, Science 341 (2013) 1230444.
[20] J.D. Xiao, Q. Shang, Y. Xiong, Q. Zhang, Y. Luo, S.H. Yu, H.L. Jiang, Angew. Chem. 128 (2016) 1–6.
[21] A. Aijaz, A. Karkamkar, Y.J. Choi, N. Tsumori, E. Ronnebro, T. Autrey, H. Shioyama, Q. Xu, J. Am. Chem. Soc. 134 (2012) 13926–13929.
[22] J.Y. Han, D.P. Wang, Y.H. Du, S.B. Xi, J.D. Hong, S.M. Yin, Z. Chen, T.H. Zhou, R. Xu, J. Mater. Chem. A 3 (2015) 20607–20613.
[23] Y. Su, Y. Ao, H. Liu, Y. Wang, J. Mater. Chem. A 5 (2017) 8680–8689.
[24] M. Müller, S. Hermes, K. Kähler, M.W.E.V.D. Berg, M. Muhler, R.A. Fischer, Chem. Mater. 20 (2008) 4576–4587.
[25] D. Wang, Z. Li, J. Catal. 342 (2016) 151–157.
[26] D. Wang, Y. Pan, L. Xu, Z. Li, J. Catal. 361 (2018) 248–254.
[27] D. Sun, Z. Li, C, J. Phys. Chem. 120 (2016) 19744–19750.
[28] D. Sun, M. Xu, Y. Jiang, J. Long, Z. Li, Small Methods (2018) 1800164.
[29] Z.G. Gu, D.J. Li, C. Zheng, Y. Kang, C. Wöll, J. Zhang, Angew. Chem. Int. Ed. 56 (2017) 6853–6858.
[30] J. Aguilera-Sigalat, D. Bradshaw, Coord. Chem. Rev. 307 (2016) 267–291.
[31] A. Rahmani, H.B.M. Emrooz, S. Abedi, A. Morsali, Mater. Sci. Semicond. Process. 80 (2018) 44–51.
[32] J. He, Z. Yan, J. Wang, J. Xie, L. Jiang, Y. Shi, F. Yuan, F. Yu, Y. Sun, Chem. Commun. (Camb.) 49 (2013) 6761–6763.
[33] P.P. Bag, X.S. Wang, P. Sahoo, J. Xiong, R. Cao, Catal. Sci. Technol. 7 (2017) 5113–5119.
[34] Y. Wang, Y. Zhang, Z. Jiang, G. Jiang, Z. Zhao, Q. Wu, Y. Liu, Q. Xu, A. Duan, C. Xu, Appl. Catal., B 185 (2016) 307–314.
[35] G.A.M. Hutton, B.C.M. Martindale, E. Reisner, Chem. Soc. Rev. 46 (2017) 6111–6123.
[36] G.A.M. Hutton, B. Reuillard, B.C.M. Martindale, C.A. Caputo, C.W.J. Lockwood, J.N. Butt, E. Reisner, J. Am. Chem. Soc. 138 (2016) 16722–16730.
[37] M. Wang, J. Hua, Y. Yang, Spectrochim. Acta. A. Mol. Biomol. Spectrosc. 199 (2018) 102–109.
[38] F.M. Zhang, L.Z. Dong, J.S. Qin, G. Wei, L. Jiang, S.L. Li, L. Meng, Y.Q. Lan, Z.M. Su, H.C. Zhou, J. Am. Chem. Soc. 139 (2017) 6183.
[39] D.A. Reddy, H. Park, S. Hong, D.P. Kumar, T. Kim, J. Mater. Chem. A 5 (2017) 6981–6991.
[40] Y.K. Kim, H. Park, Energy Environ. Sci. 4 (2011) 685–694.
[41] D.Y. Hong, Y.K. Hwang, C. Serre, G. Férey, J.S. Chang, Adv. Funct. Mater. 19 (2009) 1537–1552.
[42] J. He, Z.Y. Yan, J.Q. Wang, J. Xie, L. Jiang, Y.M. Shi, F.G. Yuan, F. Yu, Y.J. Sun, Chem. Commun. 49 (2013) 6761–6763.
[43] Z.W. Wang, P.K. Nayak, J.A. Caraveo-Frescas, H.N. Alshareef, Adv. Mater. 28 (2016) 3831–3892.
[44] J. He, J. Wang, Y. Chen, J. Zhang, D. Duan, Y. Wang, Z. Yan, Chem. Commun. (Camb.) 50 (2014) 7063–7066.
[45] A. Kudo, Y. Miseki, Chem. Soc. Rev. 38 (2009) 253–278.
[46] J. Liu, X.B. Li, D. Wang, W.M. Lau, P. Peng, L.M. Liu, J. Chem. Phys. 140 (2014) 054707.
[47] M. Qiao, J. Liu, Y. Wang, Y. Li, Z. Chen, J. Am. Chem. Soc. 140 (2018) 12256–12262.
[48] A.K. Singh, K. Mathew, H.L. Zhuang, R.G. Hennig, J. Phys. Chem. Lett. 6 (2015) 1087–1098.
[49] M.R. Gholipour, T.C. Dinh, F. Béland, Nanoscale 7 (2015) 8187–8208.
[50] M. Wang, L. Cai, Y. Wang, F. Zhou, K. Xu, X. Tao, Y. Chai, J. Am. Chem. Soc. 139 (2017) 4144–4151.
[51] B. Qiu, Q. Zhu, M. Du, L. Fan, M. Xing, J. Zhang, Angew. Chem. Int. Ed. 56 (2017) 2684.
[52] A. Kongkanand, K. Tvrdy, K. Takechi, M. Kuno, P.V. Kamat, J. Am. Chem. Soc. 130 (2008) 4007–4015.
[53] J. Sun, J. Zhao, Y. Masumoto, Appl. Phys. Lett. 102 (2013) 2425.
[54] D.A. Reddy, H. Park, S. Hong, D.P. Kumar, T.K. Kim, J. Mater. Chem. A 5 (2017) 6981–6991.
[55] D. Lang, F. Cheng, Q. Xiang, Catal. Sci. Technol. 6 (2016) 6207–6216.
[56] X. Wang, J. Cheng, H. Yu, J. Yu, Dalton Trans. 46 (2017) 6417–6424.